Impact Flash Evolution of CO_2 Ice, Water Ice and Frozen Martian and Lunar Regolith-Simulant Targets

Jon D. Tandy[1]*, Mark C. Price[2], Penny J. Wozniakiewicz[2], Mike J. Cole[2], Luke S. Alesbrook[2] and Chrysa Avdellidou[3]

[1]School of Human Sciences, London Metropolitan University, London, UK, N7 8DB

[2]Centre for Astrophysics and Planetary Science, School of Physical Sciences, Ingram Building, University of Kent, Canterbury, UK, CT2 7NH

[3]Laboratoire Lagrange, Boulevard de l'Observatoire, CS 34229, 06304 Nice, France

*Corresponding author. E-mail: j.tandy@londonmet.ac.uk

The wavelength dependence and temporal evolution of the hypervelocity impact self-luminous plume (or 'flash') from CO_2 ice, water ice and frozen Martian and lunar regolith-simulant targets have been investigated using the Kent two-stage light-gas gun. An array of ten band-pass filtered photodiodes and a digital camera monitored changes in the impact flash intensity during the different phases of the emitting ejecta. Early-time emission spectra were also recorded to examine short-lived chemical species within the ejecta. Analyses of the impact flash from the varied frozen targets show considerable differences in temporal behaviour, with a strong wavelength dependence observed within monitored near-UV to near-IR spectral regions. Emission spectra showed molecular bands across the full spectral range observed, primarily due to AlO from the projectile, and with little or no contribution from vapourised metal oxides originating from frozen regolith-simulant targets. Additional features within the impact flash decay profiles and emission spectra indicate an inhomogeneity in the impact ejecta composition. A strong correlation between the density of water ice-containing targets and the impact flash rate-of-decay was shown for profiles uninfluenced by significant atomic/molecular emission, although the applicability to other target materials is currently unknown. Changes in impact speed resulted in considerable differences in the temporal evolution of the impact flash, with additional variations observed between recorded spectral regions. A strong correlation between the impact speed and the emission decay rate was also shown for CO_2 ice targets. These results may have important implications for future analyses of impact flashes both on the lunar/Martian surface and on other frozen bodies within the Solar System.

Introduction

Intense, short-lived light flashes are produced during hypervelocity impacts; indeed, flashes resulting from high-speed lunar impacts are so energetic that they are frequently observed by modest facilities (Dunham *et al.*, 2000; Cudnik *et al.*, 2003; Suggs *et al.*, 2014; Avdellidou & Vaubaillon, 2019). In order to understand the complex phenomena within such impact ejecta, laboratory measurements are utilised to more closely observe these impacts and identify the multiple, interacting processes within the rapidly evolving ejecta.

The temporal evolution of impact flashes are typically monitored in the laboratory using photodetectors (Eichhorn, 1976; Burchell *et al.*, 1996; Ernst & Schultz, 2003, 2004, 2007; Bergeron *et al.*, 2006; Lawrence *et al.*, 2006; Tsembelis *et al.*, 2008; Ernst *et al.*, 2011; Goel *et al.*, 2015; Yafei *et al.*, 2019) or high-speed cameras (Kondo & Ahrens, 1983; Schultz, 1996;

Ernst & Schultz, 2007; Schultz *et al.*, 2007; Mihaly *et al.*, 2013, 2015; Tandy *et al.*, 2014; Schultz & Eberhardy, 2015), revealing multiple phases of the radiating impact ejecta. These phases primarily comprise a rapid jet or plasma phase, a slower, expanding vapour cloud, and molten or high temperature ejecta that are dependent upon specific impact parameters (Ang, 1990; Yang & Ahrens, 1995; Kadono & Fujiwara, 1996; Schultz, 1996; Sugita *et al.*, 1998; Sugita & Schultz, 1999; Ernst & Schultz, 2004, 2007; Schultz *et al.*, 2006; Tsembelis *et al.*, 2008; Ernst *et al.*, 2011; Bruck Syal *et al.*, 2012). Several studies have also utilised spectroscopic instrumentation to further analyse the composition of the rapidly evolving ejecta plume, allowing determination of prevalent atomic and/or molecular species (Gehring & Warnica, 1963; Jean & Rollins, 1970; Schultz *et al.*, 1996, 2007; Sugita & Schultz, 1999, 2003a; Sugita *et al.*, 1998, 2003; Lawrence *et al.*, 2006; Tandy *et al.*, 2014; Schultz & Eberhardy, 2015; Verreault *et al.*, 2015).

Previous impact experiments into ices have determined the importance and degree of melting, vapourisation and ionisation within the ejecta (Timmermann & Grün, 1991; Burchell *et al.*, 1996; Schultz & Mustard, 2004; Schultz *et al.*, 2007; Bruck Syal *et al.*, 2012; Rager *et al.*, 2014). It is likely that these highly energetic impacts drastically alter the physical and chemical properties of icy bodies and could play a significant role in the evolution of planetary surface composition and the areas of space in their vicinity (Pospieszalska & Johnson, 1991; Timmermann & Grün, 1991; Burchell *et al.*, 1996; Martins *et al.*, 2013). The temporal changes in the emission and the transient chemical species generated from these frozen targets therefore warrant further investigation.

This study investigates the wavelength dependence and temporal evolution of hypervelocity impact flashes from CO_2 ice, water ice and frozen Martian and lunar regolith-simulant targets. An additional analysis of corresponding early-time emission spectra assesses contribution from specific atomic/molecular species within the initial ejecta. Variations in the observed phenomena with impact speed are also reported.

Method

A two-stage light-gas gun (Burchell *et al.* 1999) was used to horizontally accelerate 3.0 mm 7075 aluminium spheres into various frozen targets with their surface aligned at 90^o to the shot line (horizontal impact). The impact speed was selected by varying the amount of gunpowder and gas pressure in the gun's pump tube. The majority of experiments used an impact speed between 4.5 km/s and 5.0 km/s, with the exact speed measured to better than 1% for individual shots. The target chamber was evacuated to typically 50 mbar during each shot. This pressure is higher than typical vacuum conditions employed by some other impact flash experiments (e.g. Tandy *et al.*, 2014; Schultz & Eberhardy, 2015) and will reduce the mean free path of the ejecta. This will cause an increase in ablation of the high-speed ejecta, with a higher proportion of emission from the resulting high temperature vapour (Sugita & Schultz, 2003b). Consequently, the overall nature and behaviour of the observed impact flash may differ from laboratory experiments utilising lower ambient pressures. Frozen targets containing a combination of water ice, CO_2 ice and regolith simulants were prepared and compressed into 100 mm diameter, stainless steel cans, as illustrated in Figure 1.

Figure 1 – A 100 mm diameter, stainless steel can containing a frozen ~50:50 mixture of finely crushed CO_2 ice and JSC-1 Martian regolith simulant.

The chemical compositions (percentage by weight) of the JSC-1A lunar simulant (McKay *et al.*, 1994) and JSC-1 Martian simulant (Allen *et al.*, 1998) are summarised in Appendix A. The average grain size of the lunar and Martian regolith simulants are approximately 188 µm and 325 µm respectively. Targets containing ice and regolith simulant were thoroughly mixed during preparation to ensure an even distribution of materials within the target. A fine spray of water was required to bind the regolith simulants to the finely crushed CO_2 ice before refreezing the mixtures (Avdellidou *et al.*, 2017). Targets were stored at approximately -140 ^{o}C prior to impact to prevent significant CO_2 ice sublimation (for ~ 30 minutes on average). Targets were then exposed to room temperature for approximately 10 minutes whilst the impact chamber was evacuated. Given an approximate sublimation rate of 2% per hour for typical dry ice pellets, this would correspond to approximately 0.33% of the sample. However, this is likely an overestimate, as the ice is compressed within a steel with only the target surface exposed to the ambient air within the vacuum chamber (i.e. a smaller surface area). Furthermore, the sublimation of the target surface is partially dependent upon the heat transfer from the residual air, which decreases relatively rapidly once evacuation begins. Despite the relatively small loss due to sublimation, rapid thermal diffusion within the sample during evacuation would cause the target material excavated during impact to be at room temperature.

The approximate, average densities of targets containing water ice were determined by preparing multiple samples on a smaller scale (approximately 2.5 cm^3) and measuring their volume and mass using Vernier callipers and a top pan balance respectively. Densities of 0.92 g/cm^3, 1.32 g/cm^3 and 1.73 g/cm^3, were calculated for the 100% water ice, 50% water ice / 50% JSC-1 Martian regolith, and 50% water ice / 50% JSC-1A lunar regolith samples, respectively. The percentage relative standard deviation of the calculated densities were 3.4%, 4.8% and 2.0%, respectively. Densities for targets containing CO_2 ice could not be acquired using this method due to rapid sublimation during measurements. It was also not possible to determine changes in densities for targets containing CO_2 ice during evacuation of the target chamber. Approximate densities for these materials were determined by comparing emission decay data with those from targets containing water ice during subsequent analyses (detailed later). Table 1 summarises the target material and projectile speed used within each impact experiment.

SHOT ID	TARGET MATERIAL AND PERCENTAGE COMPOSITION	IMPACT SPEED (KM/S)
S1	100% CO_2 ice	4.77
S2	100% water ice	4.51
S3	50% CO_2 ice / 50% JSC-1 Martian regolith simulant	4.61
S4	50% water ice / 50% JSC-1 Martian regolith simulant	4.66
S5	50% CO_2 ice / 50% JSC-1A lunar regolith simulant	4.73
S6	50% water ice / 50% JSC-1A lunar regolith simulant	4.31
S7	100% CO_2 ice	4.92
S8	100% CO_2 ice	5.01
S9	100% CO_2 ice	4.84
S10	50% CO_2 ice / 50% JSC-1 Martian regolith simulant	4.89
S11	50% CO_2 ice / 50% JSC-1 Martian regolith simulant	4.91
S12	50% CO_2 ice / 50% JSC-1 Martian regolith simulant	4.78
S13	50% CO_2 ice / 50% JSC-1A lunar regolith simulant	4.86
S14	50% CO_2 ice / 50% JSC-1A lunar regolith simulant	4.74
S15	50% CO_2 ice / 50% JSC-1A lunar regolith simulant	4.81
S16	100% CO_2 ice	4.03
S17	100% CO_2 ice	4.85
S18	100% CO_2 ice	5.73
S19	100% CO_2 ice	5.50

Table 1 – Frozen target material and projectile speed for each impact experiment. All experiments were carried out using a horizontal impact orientation (target at 90^o to the shot line).

Impact flash decay measurements

Initial experiments monitored the impact flash intensity and decay across 10 spectral bands (between 355 nm and 950 nm) using an array of identical photodiodes with a spectral width of approximately 300 nm to 1100 nm. The photodiodes were arranged in two banks, with different optical/IR band-pass filters and encased in a protective aluminium box. The arrangement of each photodiode within the box, including the band centre, transmission efficiency and spectral width of each filter, are indicated in Figure 2. The broader spectral width (60 nm) of the 400 nm filter was utilised to capture the strong, aluminium atomic emission at 394 nm and 396 nm. The photodiode box was placed within the target chamber and positioned slightly below the shot line and approximately 650 mm from target surface, as indicated in Figure 3. Photodiodes were mounted approximately 5 mm apart with a field of view diameter of approximately 25 cm at the point of impact. Two small alignment lasers within the box were used to ensure the photodiodes' field of view (FOV) were directed at the centre of the target before each shot. The alignment accuracy was determined to be < 0.1^o. This accuracy, coupled with the large photodiode FOV, ensured each channel recorded the same impact-induced emission. The output of each photodiode was connected via an

electrical feedthrough to a high-speed data acquisition system. Triggering was achieved from the moment of impact of the discarded sabot segments onto a stop-plate with a polyvinylidene difluoride (PVDF) sensor attached. This resulted in approximately 100 µs of pre-impact data from the photodiodes before the projectile impacted the target. The resulting emission intensity data have a time resolution of 1.0 µs.

The impact flash intensities across different spectral bands for shots S1 to S6 and S16 to S19 were measured using the photodiode array. The resulting data for each spectral band was adjusted to account for the quantum efficiency of the photodiode (~0.5 across all wavelengths) and normalised according to the transmission efficiency at the central wavelength of each band-pass filter (shown in Figure 2). The inherent background voltage of each channel's baseline was then slightly raised or lowered to approximately 10.0 mV (through addition or subtraction of a specific value, independent for each channel) to allow a direct comparison of the relative intensities of each spectral band.

Additional photographs of the impact flash were recorded through a window in the target chamber approximately 1.1 m and 15˚ from the projectile shot line using a *FastCan* digital video camera (as shown in Figure 3). The camera utilised a 50 mm Nikon f1.2 lens with a resolution of 1024 x 360. As the camera was unable to be externally triggered, it was operated continuously at a frame rate of 2800 frames/s and selected frames (showing the impact flash) extracted post-shot.

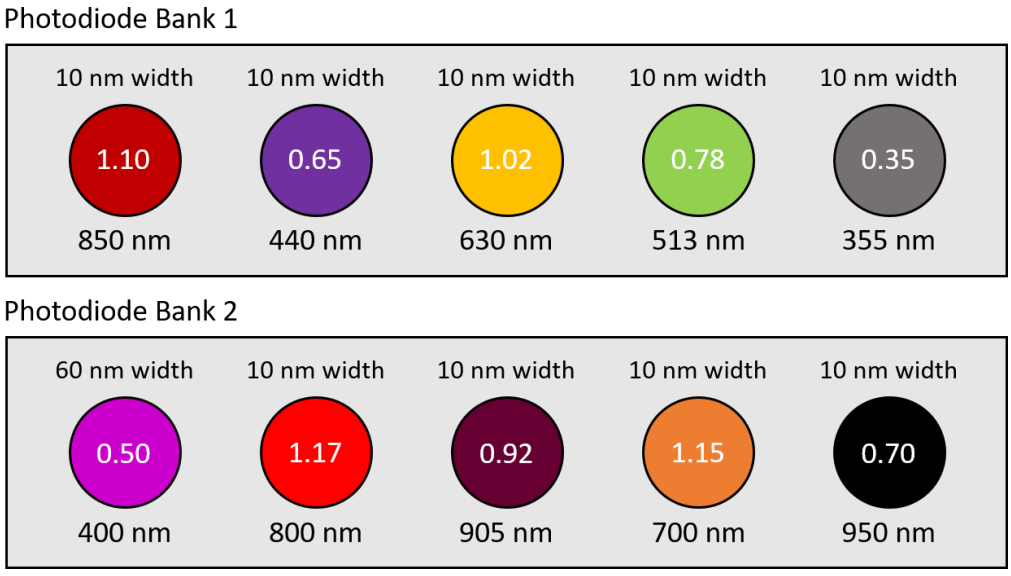

Figure 2 – Arrangement of two photodiode banks with band-pass filter spectral widths (above), transmission efficiencies (inside) and centre wavelengths (below).

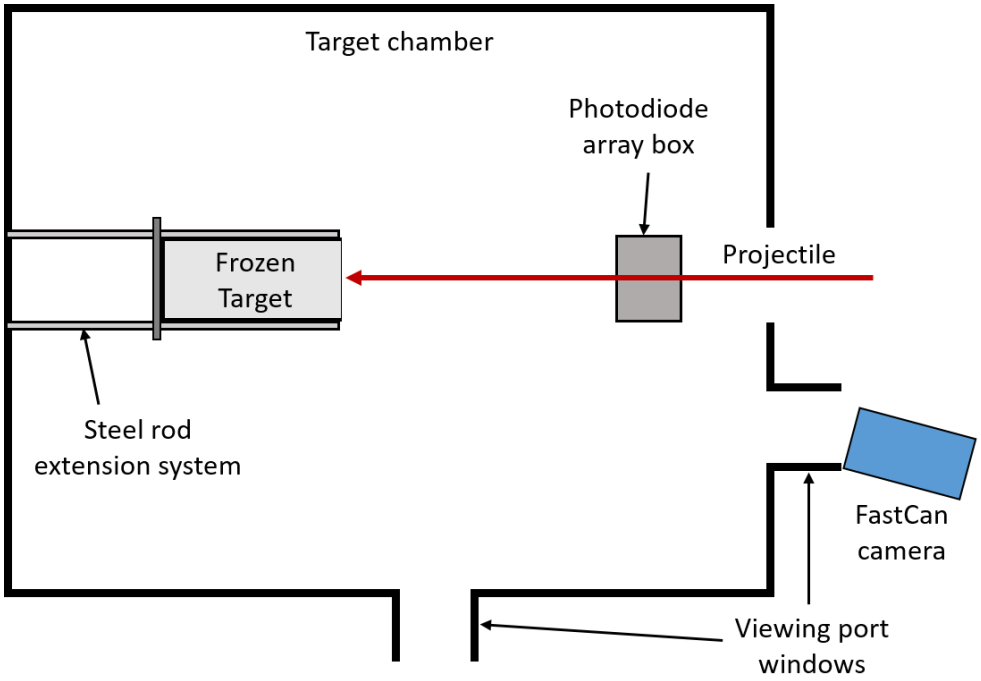

Figure 3 – Arrangement of the frozen target, photodiode array box and FastCan camera during impact flash decay measurements (not to scale).

Early-time emission spectra

Optical emission spectra of the initial impact ejecta cloud (within ~15 µs) were recorded through a side window of the impact chamber (at 90° to the shot line) using a Princeton Instruments ultra-fast, *PI-MAX4* intensified camera and *IsoPlane* spectrograph (as shown in Figure 4). A 600 g/mm diffraction grating blazed at 500 nm was utilised within the spectrometer providing a spectral width and resolution (FWHM) of approximately 60 nm and 0.2 nm respectively. Consequently, data from three individual shots (using identical impacts conditions) were combined to produce emission spectra covering a full spectral range of 470 – 640 nm. The spectral range of the three segments were 468.7 – 530.9 nm, 528.9 – 590.8 nm and 584.0 – 645.6 nm respectively. Small variations in the baseline intensity of each segment were adjusted by adding/subtracting a constant factor to slightly increase/decrease the overall intensity of the segment as required. The emission spectra were restricted to targets containing CO_2 ice and CO_2 ice/regolith mixtures, due to weak emission from the water ice targets and limited experimental time with the spectrometer system.

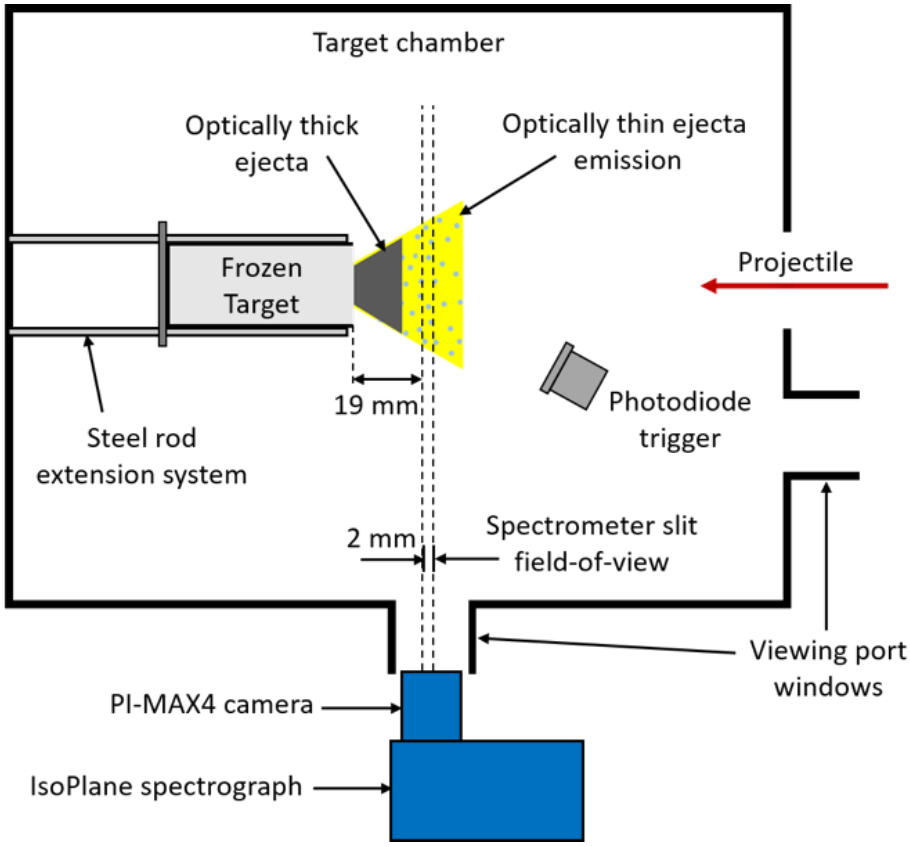

Figure 4 – Arrangement of the frozen target, IsoPlane spectrograph, PI-MAX 4 camera and photodiode trigger during early-time emission spectra measurements (not to scale). The spectrometer slit width provided a field-of-view of 2 × 91 mm (width × height) positioned 19 mm in front of the frozen target surface.

The *PI-MAX4* camera utilised a Nikon AF-S micro Nikkor 105 mm lens focussed at the centre of the target chamber. The spectrometer slit width was set to 250 µm providing a field-of-view of 2 × 91 mm (width × height) positioned 19 mm in front of the frozen target surface to minimise obscuration from fast-moving, solid/liquid ejecta during the camera exposure, as indicated in Figure 4. The system was triggered from the initial impact flash using a photodiode placed within the target chamber, approximately 150 mm from the target (shown in Figure 4). The camera exposure time was set to 10 µs with the trigger delay time (response delay from the photodiode) dependent upon the target. The average variation in the trigger delay for each target material was ±0.9 µs. Previous work using similar impact conditions showed that the ejecta present within the first microsecond is typically optically thick (Heunoske *et al.* 2013). Fortunately, the trigger delay within these experiments effectively ensured that all spectra measured optically thin ejecta and exclusively observed spectra in emission.

Results

Preliminary impact flash measurements showed reproducible temporal behaviour of the individual photodiodes, allowing a comparison between channels. Figure 5 shows the impact flash decay of each photodiode over the first 2 ms for a pure CO_2 ice target (shot S1) indicating variation across the different spectral bands. Additionally, Figure 6 shows three sequential *FastCan* camera images (exposure time approximately 0.35 ms) corresponding to frames in which the impact emission was visible during shot S1.

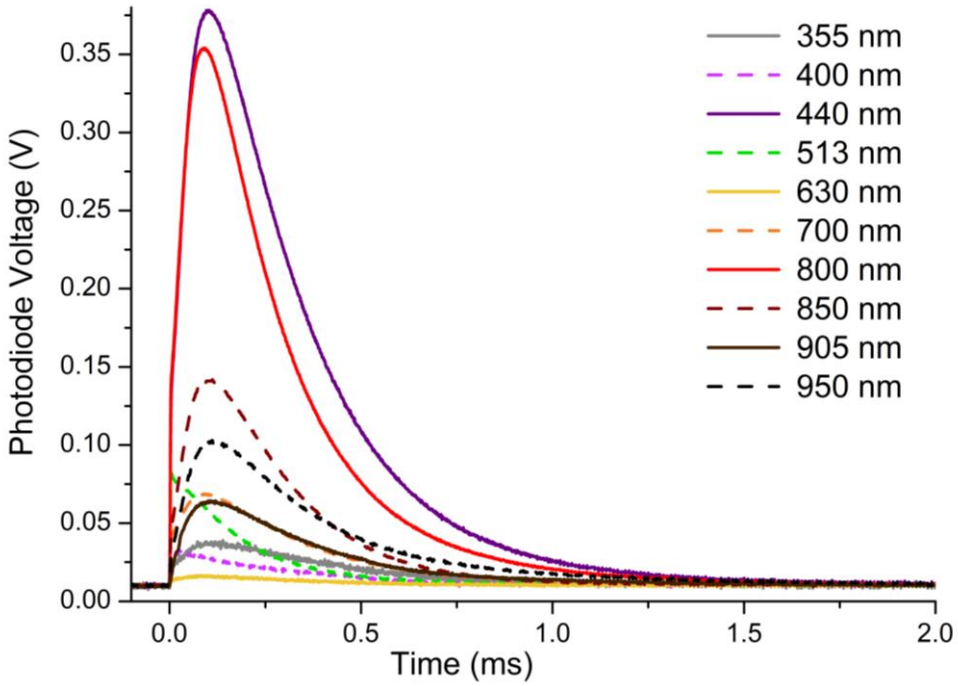

Figure 5 – Impact flash decay measurements over 10 spectral bands from a 3 mm Al projectile impacting a solid CO_2 ice target at 4.77 km/s. The wavelengths shown are the central wavelengths of each band-pass filter, as indicated in Figure 2.

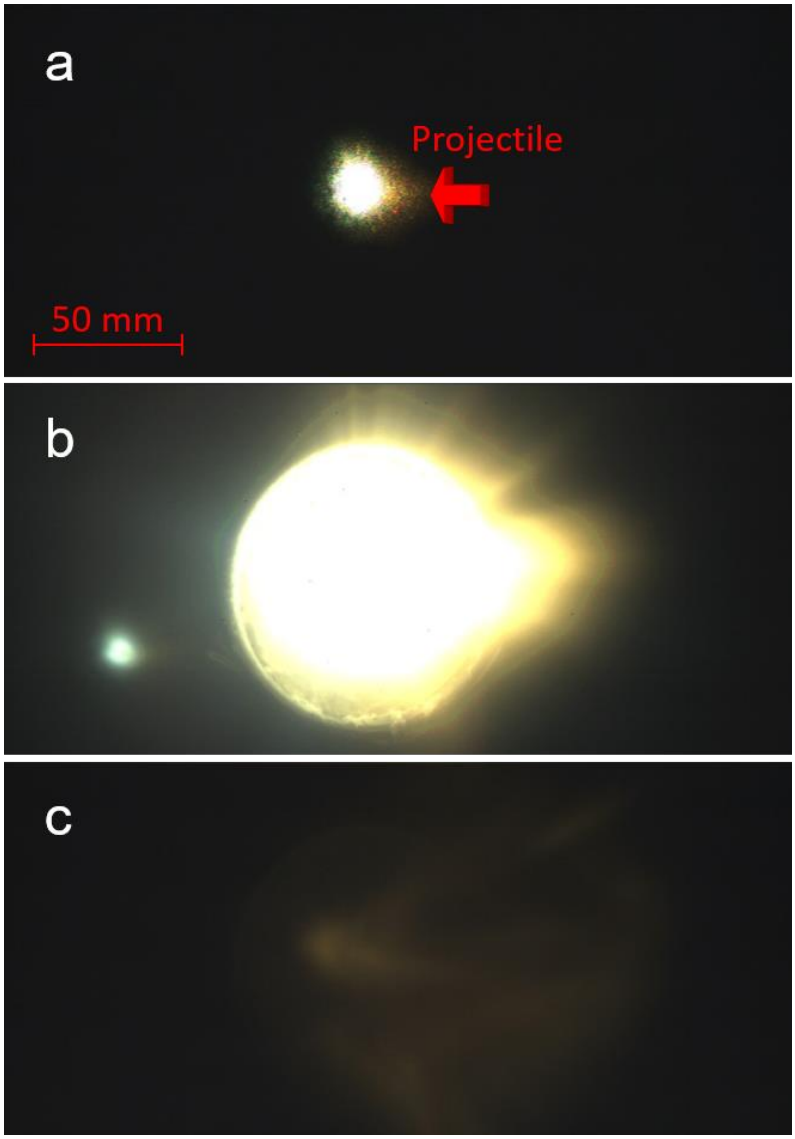

Figure 6 – Photograph sequence of the impact flash from a 3 mm Al projectile impacting a solid CO_2 ice target at 4.77 km/s. Images were acquired using a *FastCan* camera aligned approximately 15˚ from the projectile shot line, operating at 2800 frames/s, corresponding to an exposure time of ~0.35 ms. Exact timings of each frame relative to the impact time could not be acquired due to the inability to externally trigger the camera. The bright area on the left side of image b) is due to specular reflection from the steel can containing the frozen target. The edge of the steel can is also observed as the circular feature in image b).

A subsequent examination of the impact flash in individual photodiode channels for different target materials indicated considerable variation in both the peak intensity and decay profiles of the ejecta emission. Furthermore, these variations were shown to be different for specific spectral bands. This is illustrated in Figure 7, which shows the variation in impact flash decay profiles of the six target materials for all photodiode channels except those with filters centred at 400 nm and 630 nm (note the differences in the voltage scale for each channel). The 400 nm channel was not used for this comparison due to the different spectral width of the band-pass filter (60 nm in comparison to 10 nm for all other filters). The 630 nm photodiode data was also not included due to the extremely low intensities consistently measured by this channel.

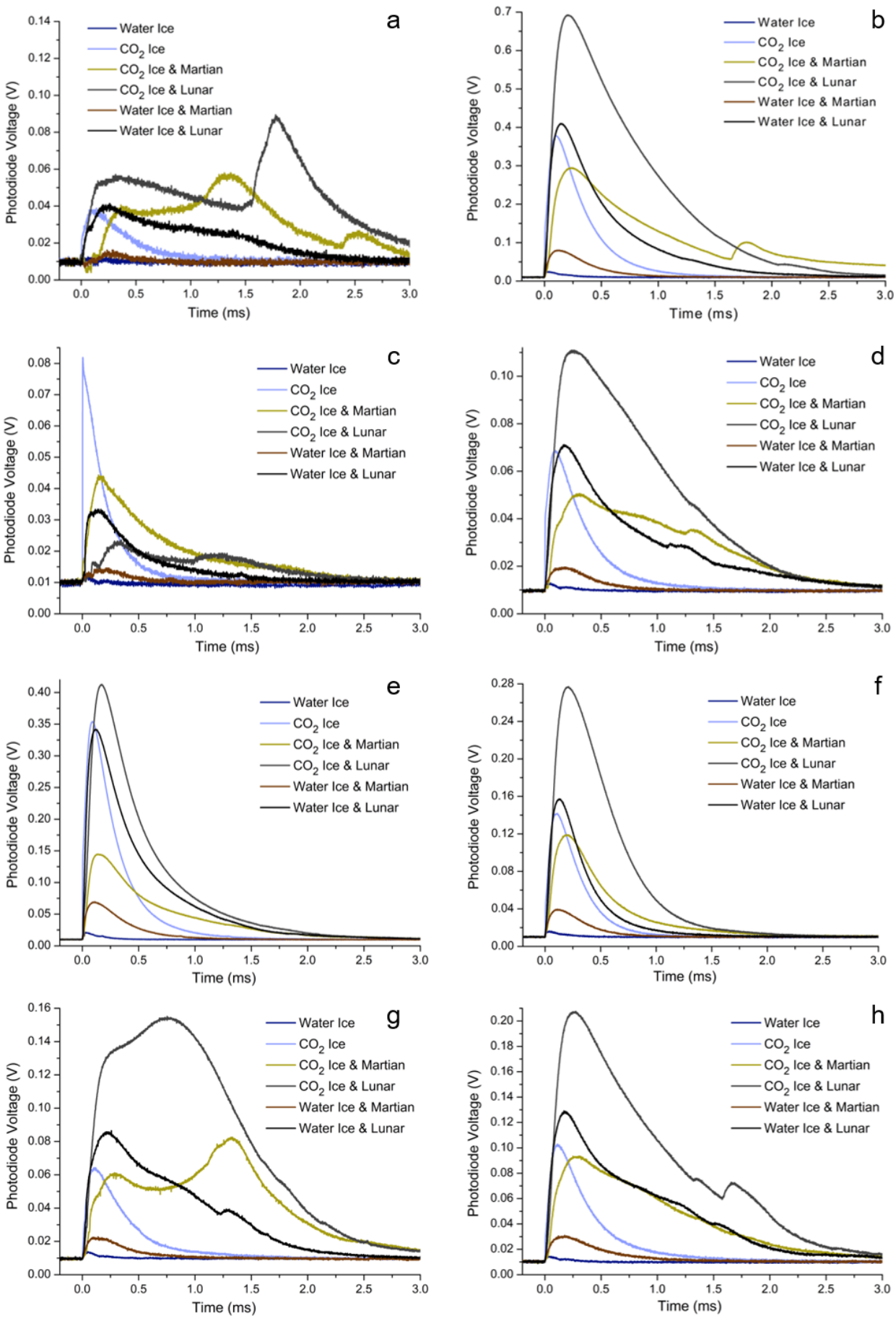

Figure 7 - Impact flash decay measurements from a 3 mm diameter Al projectile impacting six different target materials, as indicated in Table 1 (shots S1-S6). The central wavelengths of the eight spectral bands shown are a) 355 nm, b) 440 nm, c) 513 nm, d) 700 nm, e) 800 nm, f) 850 nm, g) 905 nm and h) 950 nm respectively.

Despite variations in temporal behaviour between targets, Figure 7f) shows a uniform decay profile for all materials. This data was used to calculate decay exponents (α) for each material using the method outlined by Ernst and Schultz (2003) with the resulting decay curves shown in Figure 8.

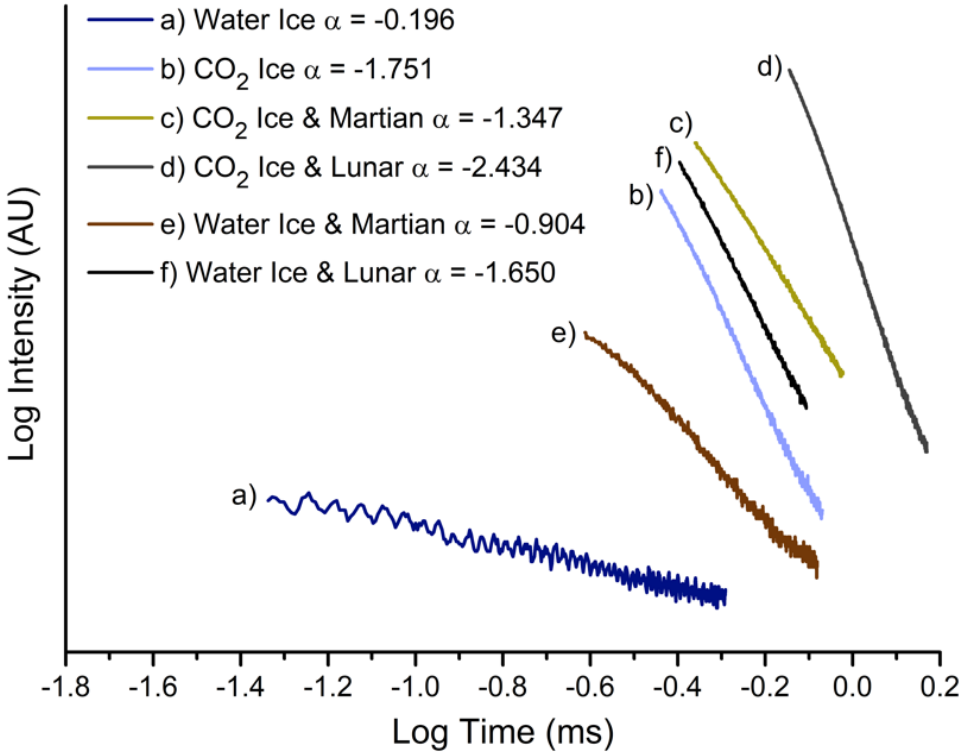

Figure 8 – Decay curves and corresponding decay exponents (α) using the 850 nm photodiode data for each frozen target.

Decay exponents obtained for each water-containing target showed a strong correlation to the measured target densities, as shown in Figure 9. Equivalent data points were not plotted for CO_2-containing targets, as accurate density values could not be determined due to rapid sublimation during measurements.

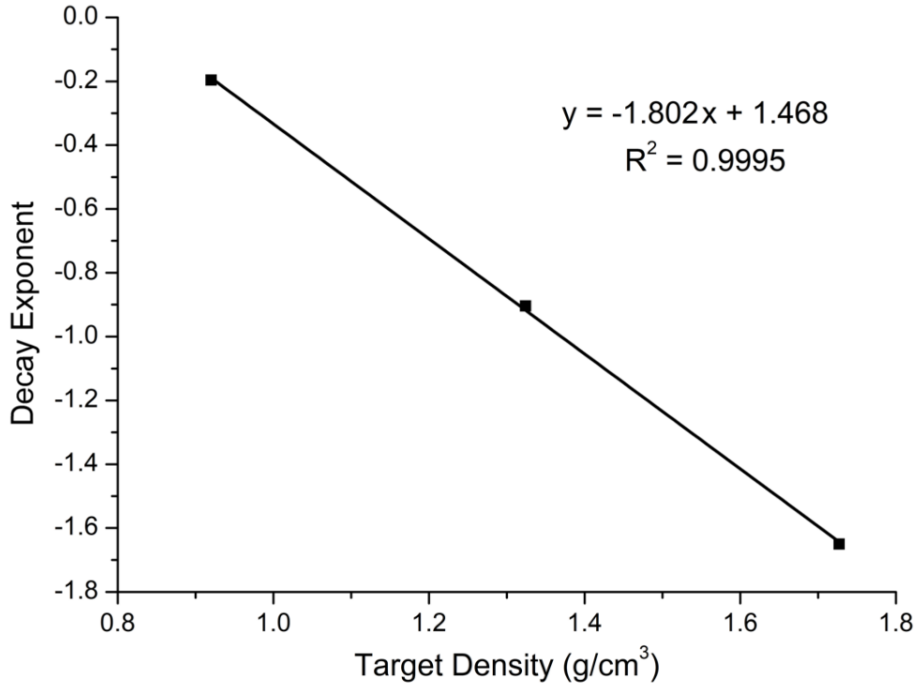

Figure 9 – Decay exponent (α) versus target density for 100% water ice, 50% water ice / 50% Martian regolith simulant, and 50% water ice / 50% lunar regolith simulant targets. The best-fit equation indicates a linear relationship.

An analysis of the variation in decay profile with impact speed was also undertaken. Figures 10, 11 and 12 compare the flash decay profiles from shots S16 to S18 for the 440 nm, 513 nm and 630 nm photodiode channels respectively.

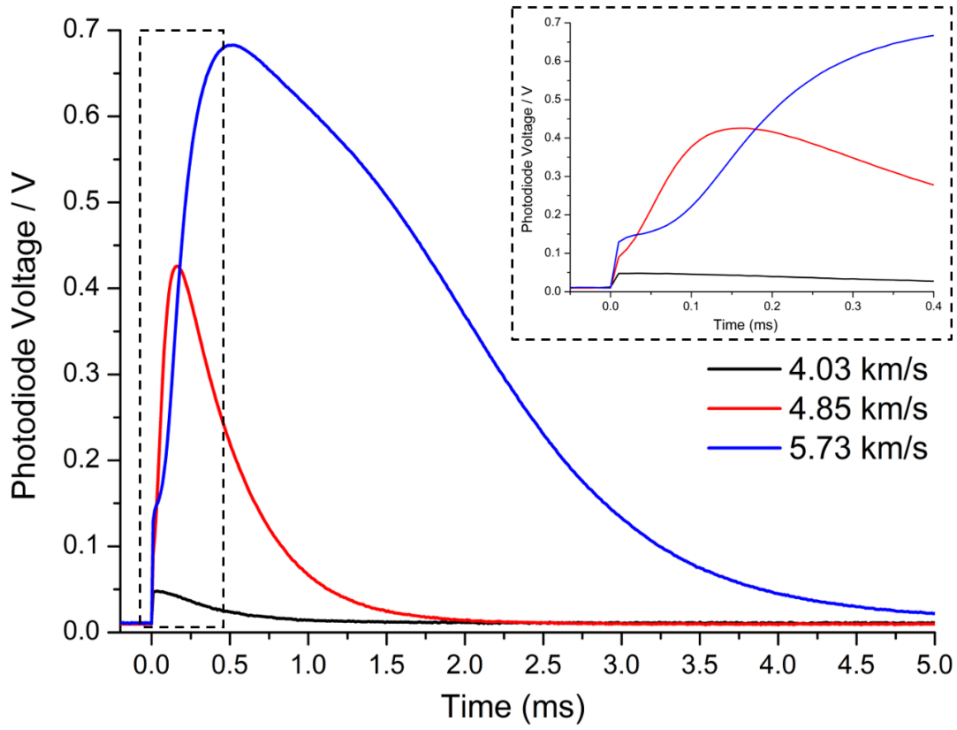

Figure 10 – Impact flash measurements of the 440 nm photodiode channel for a 3 mm diameter Al impact onto a CO_2 ice target at three different impact velocities. The insert in the top right of the figure shows the difference in emission profile within the first 0.4 ms.

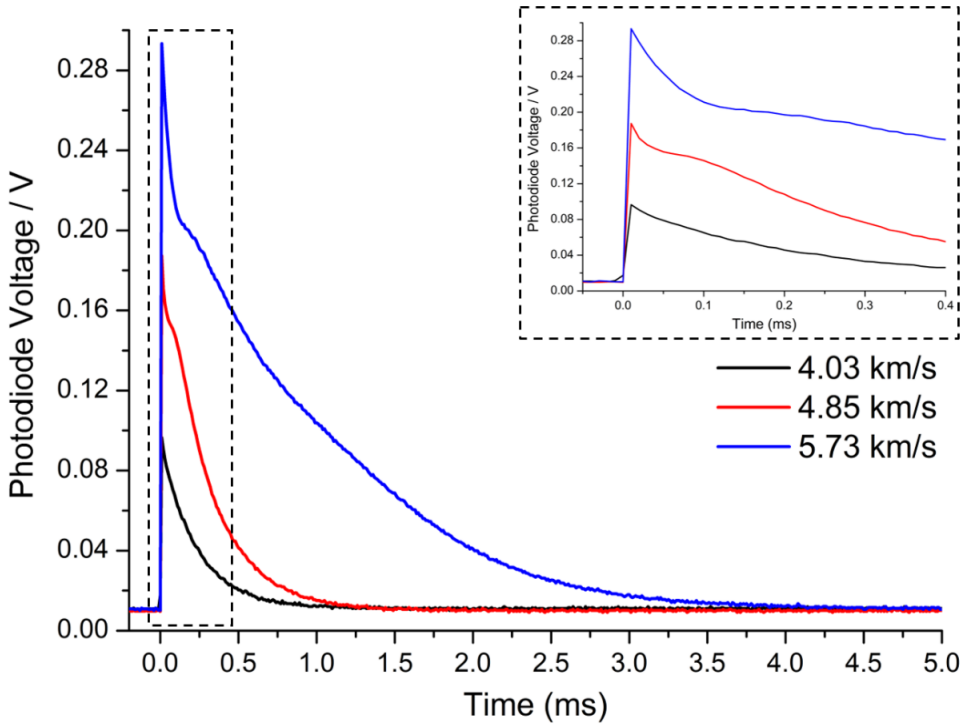

Figure 11 – Impact flash measurements of the 513 nm photodiode channel for a 3 mm diameter Al impact onto a CO_2 ice target at three different impact velocities. The insert in the top right of the figure shows the difference in emission profile within the first 0.4 ms.

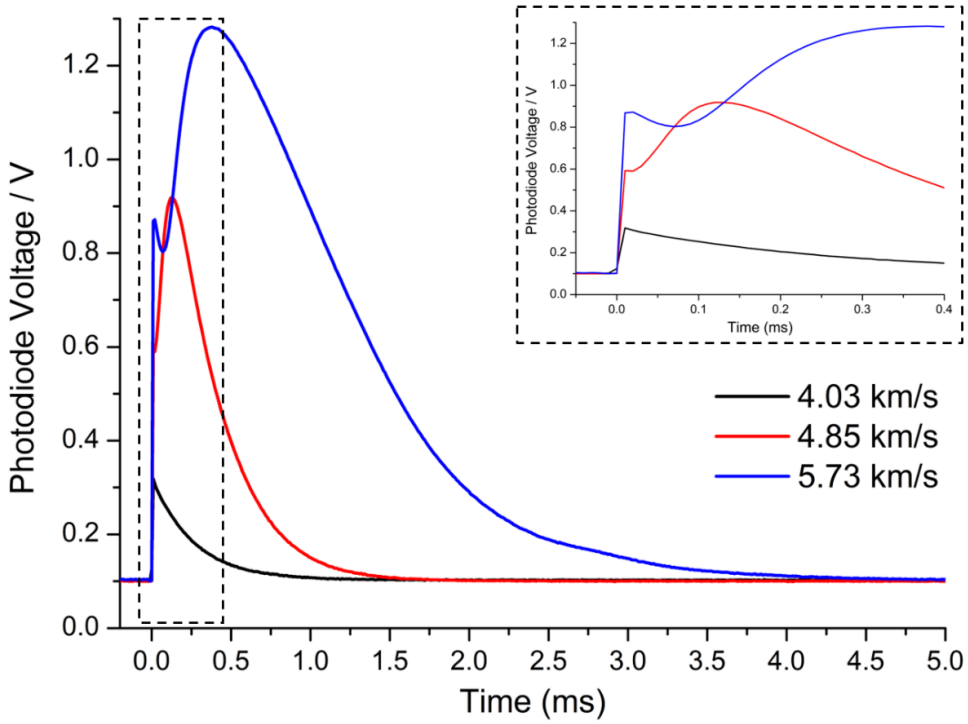

Figure 12 – Impact flash measurements of the 630 nm photodiode channel for a 3 mm diameter Al impact onto a CO_2 ice target at three different impact velocities. The insert in the top right of the figure shows the difference in emission profile within the first 0.4 ms.

Decay exponents (α) for four CO_2 ice impacts at varied impact speeds (shots S16 to S19) were calculated using the 850 nm photodiode channel measurements. These α values showed a strong correlation to the impact speed, as shown in Figure 13.

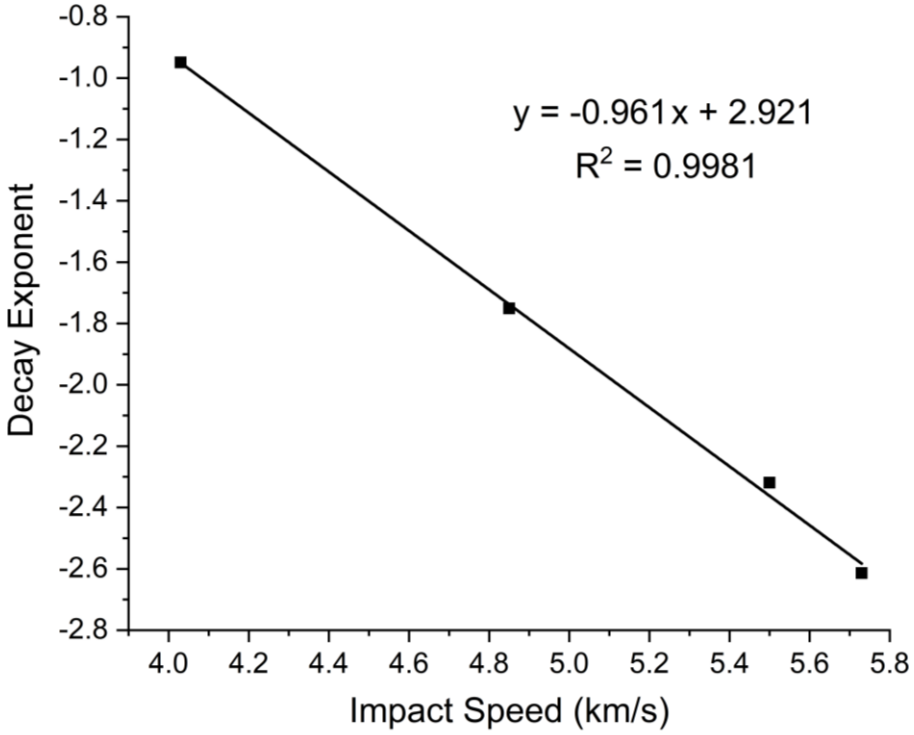

Figure 13 – Decay exponent (α) versus impact speed for 100% CO_2 ice targets. The best-fit equation indicates a linear relationship.

Early-time emission spectra were also recorded and combined (as described in the methods) for pure CO_2 ice (shots S7 to S9), CO_2 ice & Martian regolith (shots S10 to S12) and CO_2 ice & lunar regolith (S13 to S15) targets, which are shown in Figures 14, 15 and 16 respectively.

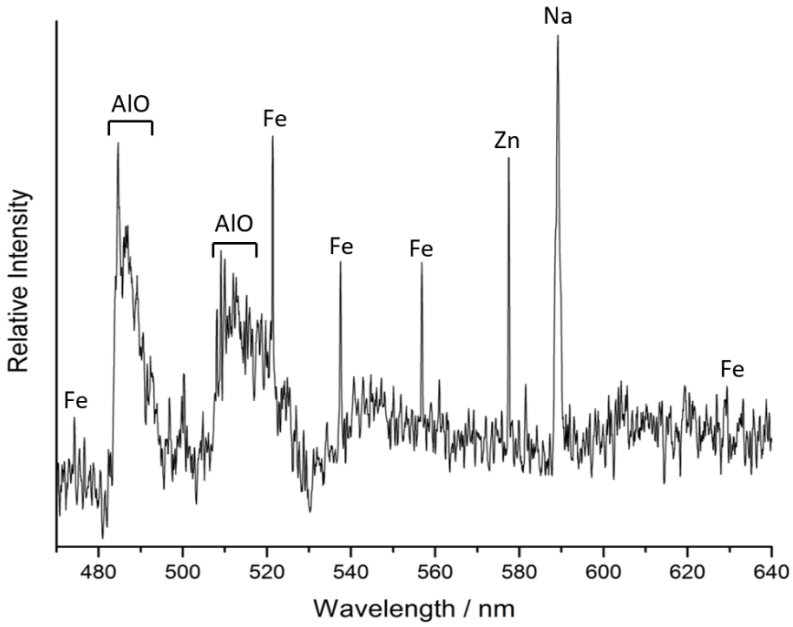

Figure 14 – Emission spectrum of a 3 mm 7075 Al projectile impacting a solid CO_2 ice target using a camera exposure time of 10 µs. The spectrum comprises data from shots S7, S8 and S9 (468.7 – 530.9 nm, 528.9 – 590.8 nm and 584.0 – 645.6 nm respectively) with trigger delay times of 2.5 µs, 1.4 µs and 2.1 µs respectively. Atomic/molecular assignments of the major emission lines/bands are indicated above. Observed Fe lines are most likely impurities originating from the stainless steel can.

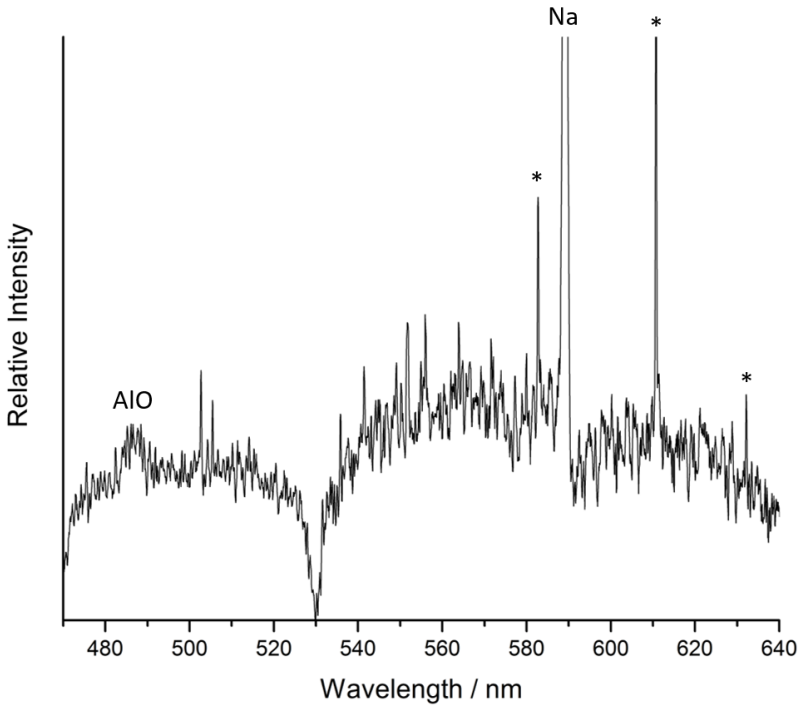

Figure 15 – Emission spectrum of a 3 mm diameter 7075 Al projectile impacting a solid 50% CO_2 ice / 50% Martian regolith simulant using an exposure time of 10 µs. The spectrum comprises data from shots S10, S11 and S12 (468.7 – 530.9 nm, 528.9 – 590.8 nm and 584.0 – 645.6 nm respectively) with trigger delay times of 7.2 µs, 7.3 µs and 9.9 µs respectively. Atomic/molecular assignments of the major emission lines/bands are indicated above. The full intensity of the Na atomic emission line at ~ 590 nm is not shown to allow weaker emission lines/bands to be seen.

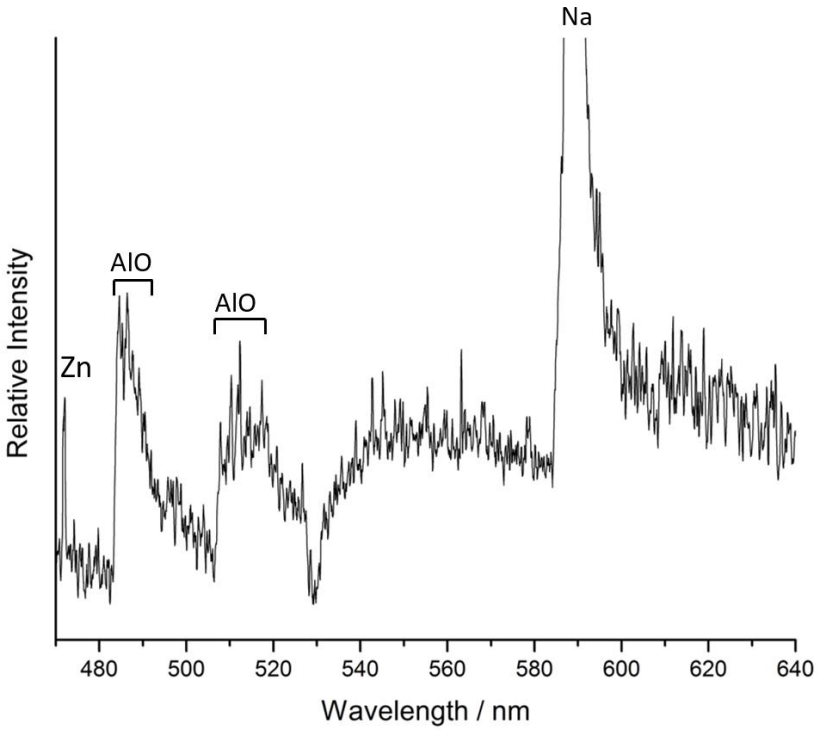

Figure 16 – Emission spectrum of a 3 mm diameter Al projectile impacting a solid 50% CO_2 ice / 50% lunar regolith simulant using an exposure time of 10 µs. The spectrum comprises data from shots S13, S14 (468.7 – 530.9 nm, 528.9 – 590.8 nm and 584.0 – 645.6 nm respectively) and S15 with trigger delay times of 4.5 µs, 5.5 µs and 4.9 µs respectively. Atomic/molecular assignments of the major emission lines/bands are indicated above. The full intensity of the Na atomic emission line at ~ 590 nm is not shown to allow weaker emission lines/bands to be seen.

Further analysis of the data revealed differences in the emission spectrum in different areas of the camera CCD, corresponding to different vertical positions within the ejecta. The CO_2 ice impact data was subsequently binned into 15 segments (rows of CCD pixels) corresponding to a field-of-view of approximately 2 × 6 mm (width × height). Figure 17 indicates the different emission spectra of shot S7 for two of these segments showing the strongest emission.

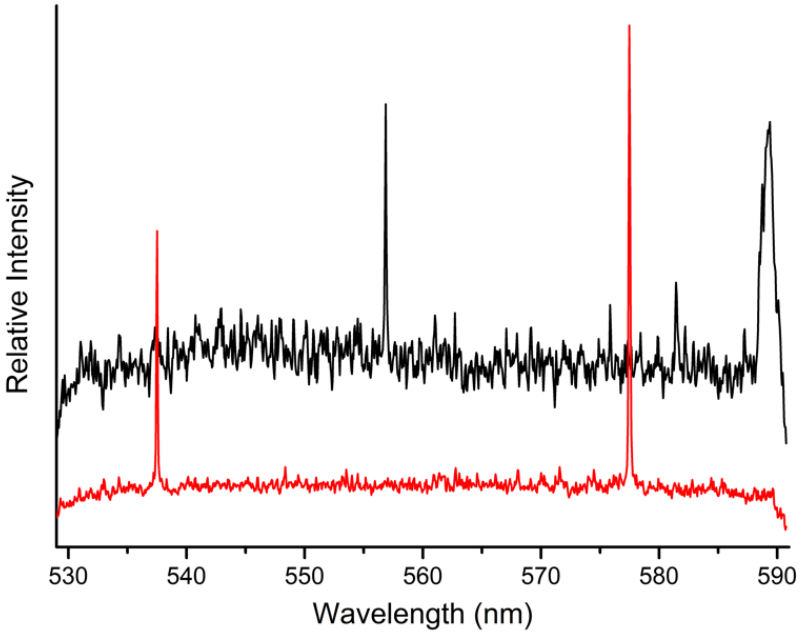

Figure 17 – Emission spectra of two data segments originating from shot S7 using a camera exposure time of 10 µs with a trigger delay time of 1.4 µs.

Discussion

The impact flash decay observed across the different spectral channels shown in Figure 5 indicates a variation in both in the peak intensity and temporal behaviour of the emission. Although normalised for photodiode quantum efficiency, it is difficult to provide a fully quantitative comparison of the peak flash intensity across the different channels, as the photodiode array was not calibrated to take into account additional variations between photodiodes (e.g. sensitivity, filter efficiency, etc.). Indeed, a precise, quantitative analysis of the peak emission across the spectral bands covered by each photodiode is beyond the scope of this article. Nevertheless, the photodiode data suggests that certain spectral regions (e.g. around 440 nm and 800 nm) emit more in the initial 250 µs than others (e.g. around 400 nm and 630 nm).

Figure 5 also shows that, in general, the emission decay profile is similar in the majority of the photodiode channels and returns the baseline at around 1.5 ms. The figure also indicates that most channels peak between approximately 70-100 µs after impact. The observed emission should be primarily due to thermal radiation from the hot, expanding gas cloud present after the initial jetting phase. The uniformity in the majority of decay profiles is consistent with a cooling blackbody within an expanding gas cloud (Ernst & Schultz, 2004; Schultz & Eberhardy, 2015). Figure 6 illustrates this rapid expansion and cooling of the ejecta within the sequence of impact flash photographs and indicates that the increase in photodiode

intensities to their peak is primarily due to an expansion of the radiating area exposed to the detectors.

A similar study by Ernst and Schultz examined the peak emission intensity during spherical Pyrex impacts into pumice dust targets using six calibrated photodiodes with various band-pass filters (Ernst and Schultz, 2004). The resulting data showed the maximum intensities for the filtered photodiodes to be approximately the same, with no clear trend between wavelength and peak emission intensity. Conversely, Yafei *et al.* observed considerable variation in the peak intensities of four photodiodes monitoring different wavelengths (400 nm, 500 nm, 600 nm and 700 nm) during impacts of Al projectiles onto Al plates (Yafei *et al.*, 2019). This suggests that the projectile and/or target materials play a pivotal role in the relative strength of the emission across the visible and near-IR spectrum.

Figure 5 also shows inconsistencies in the integrated intensities and peak times between photodiodes. Two notable exceptions are the 400 nm and 513 nm channels, which peak at 25 µs and 4 µs, respectively. Analyses by Ernst and Schultz of impact emission decay using photodiodes concluded that the overall impact flash decay time primarily provides information regarding the physical nature of the target's surface, whereas the peak emission time is related to the properties of the impactor (Ernst & Schultz, 2003). This implies that the observed variation in peak intensity time in these two channels is likely linked to atomic/molecular emission involving aluminium. Figure 14 shows that one of the strongest emission bands in the observed spectrum is due to AlO between approximately 508 nm to 525 nm, coinciding with the spectral range of the photodiode channel centred at 513 nm. Additionally, the photodiode centred at 400 nm would capture the strong Al atomic emission lines at 394.4 nm and 396.2 nm. These Al/AlO emission lines/bands have been observed in previous impact experiments (Schultz, 1996; Schultz *et al.*, 1996; Heunoske *et al.*, 2013; Tandy *et al.*, 2014; Verreault *et al.*, 2015) and all other Al atomic and AlO molecular emission would fall outside of the spectral regions covered by the remaining photodiodes. Yafei *et al.* (2019) also observed an earlier peak in the decay profile for the band-pass filtered photodiode centred at 400 nm, which would capture the aforementioned Al atomic emission.

Schultz first measured the impact-induced emission spectrum from a dry ice target (Schultz, 1996) and primarily observed AlO emission bands, from rapid impactor/target reactions within the ejecta cloud, and a strong Na atomic emission line at ~590 nm commonly observed from projectile impurity vapourisation in impact experiments (e.g. Sugita *et al.*, 2003; Tandy *et al.*, 2014; Schultz & Eberhardy, 2015). Figure 14 indicates that the same spectroscopic features are detected in this study, with strong AlO molecular emission between 484 nm and 525 nm (Pearson & Gaydon, 1976) and a strong Na atomic line at 589.2 nm (Kramida *et al.*, 2020). Additional atomic/molecular emission lines/bands deriving from various sources are also observed. The Zn atomic emission line at ~578 nm originates from the projectile (7075 aluminium contains approximately 6% zinc), whilst multiple Fe lines are most likely impurities originating from the stainless steel can. Additional, weaker bands are also seen throughout the spectrum but cannot be conclusively assigned to specific atomic/molecular species.

One might expect CO bands from vapourised CO_2 ice target material to also be observed in emission. These bands have been previously detected in several other impact experiments using a variety of projectile and target materials (Schultz, 1996; Schultz *et al.*, 2007; Schultz

& Eberhardy, 2015). Three band heads of CO that are potentially evident within Figure 14 are the $0-1$, $0-2$ and $0-3$ $(\mathrm{v}'-\mathrm{v}'')$ $B^1\Sigma - A^1\Pi$ vibronic transitions, at 483.5 nm, 519.8 nm and 561.0 nm respectively (Pearse & Gaydon, 1976). However, additional spectroscopic measurements for this projectile-target system would be required to conclusively assign these bands due to their very low intensities.

The significant difference in the spectral bands shown in Figure 17 (corresponding to different vertical positions within the radiating plume) may explain slight inconsistencies in the emission spectra of shots S7 to S9, where certain lines or bands may have been expected to be more/less intense. For example, the relative intensity of the Fe lines observed in these spectra are not completely consistent with the Einstein coefficients for these transitions. Indeed, one might expect other strong Fe lines (e.g. at ~532 nm) to be observed within the spectral region covered by Figure 14 if the impact energy was evenly distributed throughout the radiating ejecta. The observed variation in emission within the ejecta may therefore provide an explanation for these slight inconsistencies. Sugita and Schultz (1999) also proposed that self-absorption of opaque, fine-grained debris/droplets may be responsible for inconsistent atomic emission intensities, which would likely exhibit strong blackbody radiation. Given the relatively low background shown in Figure 17, it seems unlikely this is primary cause of the observed intensity variations. Additionally, it is possible that the specific transitions measured in the current study provide a preferential decay pathway for the atomic/molecular species to dissipate their internal energy within the expanding ejecta cloud.

The mixed CO_2 ice and Martian regolith spectrum in Figure 15 shows a significant reduction in the AlO and Zn emission in comparison to the pure CO_2 ice target spectrum. Other weak emission features are also observed at approximately 582.7 nm, 610.6 nm and 632.0 nm (indicated by an asterisk). These bands cannot be conclusively assigned, but approximately correspond to emission bands of FeO, CuO and MgO respectively (Pearson & Gaydon, 1976), which could potentially originate from metal oxides within the Martian regolith, although these assignments are extremely tentative. Interestingly, mixed CO_2 ice and lunar regolith spectrum in Figure 16 shows a slight increase in AlO emission in comparison to Figure 15, but shows no evidence of any bands corresponding to metal oxide emission.

The reduced projectile emission observed in Figures 15 and 16 correlate with an increase in trigger delay time of the spectrometer, with the lowest AlO emission for the Martian regolith-containing target corresponding to the largest average trigger delay. This observation is consistent with the most intense projectile emission occurring during the short-lived jetting phase immediately after impact (Sugita & Schultz, 1999; Schultz & Eberhardy, 2015). The apparent disappearance of the bands potentially corresponding to FeO, CuO and MgO in Figure 16 might be explained by the reduction in metal oxide composition (except for CaO) within the lunar regolith simulant (Appendix A).

The relative proportion of emission lines/bands originating from the projectile and target materials at different stages after impact has been previously investigated (Sugita & Schultz, 1999; Schultz & Eberhardy, 2015;). Schultz and Eberhardy (2015) concluded that, at distances relatively close to the point of impact, early-time emission spectra (within the first 20 µs after impact) are dominated by projectile emission caused by high speed jetting. Given the short exposure time and positioning of the spectrometer system, the strongest

lines/bands within emission spectra of this study should therefore originate from the projectile, which is confirmed by the relative intensities in Figure 14. Sugita *et al.* (2003, 2004) showed the relative intensity of such optical emission is strongly controlled by the partition function and the degrees of electronic excitation and ionisation. Furthermore, the specific electronic excitation energies were shown to govern the relative intensities between emission lines from identical elements, and the degree of ionisation shown to primarily control the intensity ratio of emission lines between different atomic species. The apparent lack of clear spectral signatures other than AlO indicates that the majority of the emitting species within the self-luminous plume originate from the aluminium projectile, with little or no contribution from vapourised species from the target material. This may be due to insufficient energy from the relatively small-scale impact to ionise or electronically excite the necessary quantity of target material. The spectra also show little evidence of an underlying high temperature, blackbody background, suggesting that the detected ejecta/condensates (originating from the vapour plume) are relatively cool. This is expected given the position of the spectrometer, which would allow considerable expansion and cooling of this material before entering the specific field-of-view of the *PI-MAX4* camera (Figure 4).

Figure 7 illustrates the considerable differences in the relative peak emission for the various target materials within each photodiode channel. Despite these deviations, a few general conclusions can be made (when using aluminium projectiles):

1. The average peak emission intensity of the 100% water ice is considerably lower than the other targets.
2. The average peak emission intensity is higher when using CO_2 ice (rather than water ice) within the target.
3. The average peak emission intensity is higher for targets containing the lunar regolith simulant in comparison to the Martian regolith simulant.
4. The primary emission peak occurs slightly later for targets containing lunar or Martian regolith simulant.

The *FastCan* camera photographs in Appendix B (recorded for shots S1, S2, S5 and S6) also confirm the general trend that targets containing CO_2 ice yield brighter impact flashes in comparison to those that contain water ice.

These trends may potentially be explained by the relative densities of the different target materials: the measured densities for the water-containing targets show an increase in density from pure water ice to frozen Martian regolith to frozen lunar regolith, and CO_2 ice has a higher density (between 1.4 g/cm^3 and 1.6 g/cm^3 from Haring *et al.*, 2007) than water ice. The delayed emission peak of the regolith containing targets could also be explained by the increased obscuration caused by the ejecta from these materials. A higher proportion of the pure ice targets (water or CO_2) will be vapourised upon impact, meaning a reduction in the solid debris obscuring the initial flash. Ejecta from regolith-containing targets would therefore need to expand further before the maximum emission intensity could be detected by the photodiode array.

The range of decay exponent (α) values shown in Figure 8 reflects the considerable variation in the properties of the six target materials and correlates well with the general trends observed for the peak emission intensities:

1. The relative rate of decay of the 100% water ice emission is considerably longer than the other targets.
2. The relative rate of decay is shorter when using CO_2 ice (rather than water ice) within the target.
3. The relative rate of decay is shorter for targets containing the lunar regolith simulant in comparison to the Martian regolith simulant.

The α values of the mixed water ice and lunar/Martian regolith-simulant targets also compare favourably with the decay exponent obtained by Ernst and Schultz for a frozen perlite target (α = -1.02 from Ernst & Schultz, 2003).

Figure 9 shows a strong, linear correlation between the decay exponent and target density (for water ice-containing targets), with α decreasing for increasing target density, as previously noted by Ernst and Schultz for sand, pumice and perlite targets (Ernst & Schultz, 2003). Their examination of frozen and unfrozen perlite targets also showed a greater excavation efficiency in particulate targets, corresponding to a smaller α (longer rate of decay) for the unfrozen sample. The Martian regolith containing targets of this work were observed to break apart much more easily during preparation, with the mixed CO_2 ice and Martian regolith targets requiring slightly more water to effectively bind the materials. The greater particulate nature of the Martian regolith containing targets (in comparison to the lunar regolith) is likely related to the larger average grain size and are also reflected in the considerably smaller α values shown in Figure 8. A future study examining the correlation between grain size distribution and decay exponent is therefore warranted to ascertain the importance of this parameter in the emission decay for various target materials.

Despite the strong correlation between decay exponent and target density observed, several factors are known to contribute to the impact flash decay. Firstly, the porosity of the target has been shown to significantly alter the emission decay and duration (Ernst & Schultz, 2003, 2007; Schultz *et al.*, 2005) with highly porous particulate targets reducing the flash lifetime by more than two orders of magnitude. Although it is difficult to assess the exact porosity of the frozen, mixed ice and regolith targets, the average grain size for the Martian regolith simulant used in this study was considerably larger than the lunar simulant, which may correlate to a decreased porosity within the frozen targets. This would imply a slower emission decay in the Martian regolith containing targets in comparison to those containing lunar regolith, which is supported by the alpha values shown in Figure 8. However, the precise correlation between grain size and porosity upon impact for frozen targets has not been established meaning a clear correlation between porosity and decay exponent cannot be determined for the target materials used in this study. Indeed, the simulants used do not reflect the true grain size distribution for either Martian or Lunar regolith, but were utilised for their chemical similarity. It is also likely that the relative composition of the mixed ice regolith targets would affect this parameter and should be investigated further to examine a possible correlation between decay exponent and the percentage of regolith used within the frozen target. Secondly, the

difference between solid and particulate targets has been shown to reduce peak emission duration by a factor of two (Ernst & Schultz, 2007). Given that all targets within this study were frozen into a solid block, it seems likely that this parameter should not have significantly affected the measured decay exponents.

Thirdly, the volatile content of the target is also understood to influence the blackbody radiation that contributes towards the impact flash lifetime (Ernst & Schultz, 2003; Schultz *et al.*, 2005). An increased volatile content generally yields a greater radiant energy for a volatile-rich projectile-target system like Al onto CO_2 ice. This manifests itself in the more intense AlO emission bands from the pure CO_2 ice target (Figure 14) in comparison to the mixed regolith-ice target spectra (Figures 15 and 16). If volatile content was the major factor in the determination of the decay exponent, one would expect the α value for the pure CO_2 ice to be smaller (i.e. longer decay time) than the equivalent values for the two mixed CO_2-regolith targets, as the overall heat of vapourisation/sublimation for regolith-containing targets should be considerably larger. Figure 8 illustrates that this is not the case with the pure CO_2 ice α value (-1.751) greater than the mixed CO_2 ice and Martian regolith value (-1.347), but less than mixed CO_2 ice and lunar regolith value (-2.434). However, the observed pure water ice α value (-0.196) is considerably smaller than both the mixed water ice and regolith decay exponents (Martian = -0.904 and lunar = -1.650) despite the intensity of the emission for water ice being considerably weaker (Figure 7). Additionally, the α values for the CO_2 ice-containing targets are all lower than the equivalent values for the water ice-containing targets, which fit an increased CO_2 vapour content within the ejecta plume in comparison to water vapour when using the same impact parameters. These observations suggest that an increased content of vapourised material may cause a slower decay in emission, but is likely one of several contributing factors as previously shown by Ernst and Schultz (Ernst & Schultz, 2003, 2007, 2015; Schultz *et al.*, 2005).

The decay exponents and best-fit equation of Figure 9 were subsequently used to estimate densities for the CO_2 ice containing target materials of 1.61 g/cm^3, 1.39 g/cm^3 and 1.99 g/cm^3 for the 100% CO_2 ice, 50% CO_2 ice / 50% Martian regolith, and 50% CO_2 ice / 50% lunar regolith targets, respectively, with a relative standard deviation of 2.8% (determined from the R^2 value of Figure 9). The density value determined for the 100% CO_2 ice target is in good agreement with the typical density of dry ice at room temperature (~ 1.5 g/cm^3, Haring *et al.*, 2007) suggesting that the method is relatively precise and could potentially be a useful tool to determine the composition of an unknown target material. However, considerable further investigation would be required to determine the applicability of this method for different target materials given the other contributing factors discussed above.

Additional variations were also observed in the shape of the decay profiles (Figure 7), with certain photodiode channels showing secondary peaks at times greater than 0.8 ms after impact. Indeed, three decay profiles (two in the 355 nm channel and one in the 905 nm channel) show secondary peaks with a larger emission intensity than the initial peak. Initially, one might think that these later emission peaks (generally between 0.8 ms and 1.8 ms) provide evidence of a secondary impact onto the target. If this was the case, a secondary peak should occur at approximately the same time within all photodiode channels and Figure 7 illustrates that this is not observed. Furthermore, no additional impactors (>50 microns in

size – the lower detection limit) were detected by the time-of-flight system during any of these shots. The spectral variations shown in Figure 17 also suggest that the composition of the ejecta within the first few microseconds after impact is inhomogeneous with radiating atomic/molecular species localised to specific areas. Indeed, Schultz and Eberhardy (2015) successfully measured differences in emission spectra resulting from multiple components of the ejecta/condensates passing through the field of view of their spectrometer system whilst tracking the ejecta's evolution.

One possible explanation for these secondary peaks would be due to reflected vapour phase emission from ejecta/debris that have impacted the target chamber walls. Given the shortest distance from the target to the chamber wall, a minimum ejecta/debris velocity of approximately 2 km/s would be required to produce the secondary emission at ~1 ms in the observed photodiode decay profiles. This velocity is certainly achievable given the rapidly expanding ejecta/condensate emission shown in Figure 6. The diverse range of speeds and trajectories of the reflected luminous parcels may also explain the varied timings of secondary peaks in different photodiode channels. However, it is not currently clear whether such contributions from reflected ejecta/debris would be sufficiently bright to cause observable secondary peaks within the first few milliseconds after impact.

Another potential explanation for the additional peaks could be the presence of 'pockets' of emitting material embedded within the more dense ejecta. These 'pockets' would be initially obscured from the field-of-view of each photodiode, but would become visible as the ejecta expands into the target chamber. This explanation is supported by the previously discussed segmented emission spectra, which suggests an inhomogeneous composition of the observed ejecta. This is also supported by the high-speed images of Schultz *et al.* (2007) that show small pieces of self-luminous impact melt that emerge from the growing impact crater cavity after the initial impact flash.

A third explanation is that the emission is actually generated during the expansion of the ejecta. This could potentially occur from physical and/or chemical processes within the ejecta creating emitting atomic or molecular species, or from a secondary reflected shock produced from the interface between target material and steel can. Interestingly, the secondary peaks were only observed for targets containing lunar or Martian regolith simulant, suggesting that the target composition may be critical to their occurrence. A more detailed spectroscopic study would be required to clearly understand the wavelength dependence of these secondary emission peaks and conclusively determine their origin.

Impact speed has also been shown to significantly affect the behaviour of ejecta emission. Sugita *et al.*, observed a strong dependence on impact speed for the total intensity of optical emission between 435 nm and 650 nm for copper impacts onto dolomite targets (Sugita *et al.*, 2003) and showed that the flash intensity was approximately proportional to the fifth power of impact speed, between 2 and 5.5 km/s. Previous studies by Eichhorn also showed a strong correlation between emission rise time and impact speed for iron and aluminium impacts onto tungsten and gold targets using a Van der Graff accelerator (Eichhorn, 1975 & 1976). Figure 13 indicates a similar trend for emission decay rate with a strong, linear correlation between the impact speed and decay exponent for CO_2 ice targets, with α decreasing for increasing impact speed. This observation warrants

considerable further investigation to determine if similar trends are also observed for different target materials. However, additional information can be ascertained by examining the change in emission profile with increasing impact speed.

Interestingly, the 5.73 km/s profile in Figure 12 strongly resembles that of a previously observed flash decay from a 30º, 5.7 km/s impact into sugar using a 0.64 cm Pyrex sphere (Ernst & Schultz, 2007). Figures 10-12 clearly indicate the three-component behaviour of the impact flash reported by Bergeron *et al.* (2006), Lawrence *et al.* (2006) and Ernst *et al.* (2011). These components consist of 1) an early-time spike, 2) a generally broader peak, and 3) a longer decaying signal. Previous studies have shown that the second of these components typically dominates the emission signal (Ernst & Schultz, 2004; Ernst *et al.*, 2011; Yafei *et al.*, 2019). However, Figures 10-12 indicate that this may not be the case at lower velocities, with the flash decaying immediately after the initial spike for the impact at 4.03 km/s.

Ernst *et al.* (2011) previously reported an increase in intensity of the initial spike with increasing impact speed for oblique impacts. They concluded that changes to this component correlate to an alteration in the interaction duration between projectile and target. Lower impact speeds allow a longer interaction, whilst higher impact velocities break-up the projectile more efficiently into emitting fragments. The data shown in Figures 10-12 are consistent with this explanation, with the initial component becoming more prevalent at higher impact speeds. These figures also indicate that the changes in intensity of this component are wavelength independent.

Additionally, Figures 10-12 suggest that higher impact speeds, corresponding to a greater impact energy, maintain the duration of the initial spike, but delay the peak emission intensity of the second component. The magnitude of this delay is also shown to be wavelength dependent, with the 513 nm photodiode channel exhibiting a comparatively reduced extension in the maximum intensity of the second component as impact speed increases. As previously discussed, this channel corresponds to the spectral region of strongest molecular emission, which appears to alter the behaviour of the decay profile. In the majority of photodiode channels, the temporal behaviour of the second component is primarily determined by the expansion time of the radiating ejecta cloud: the emission intensity increases to a peak as more radiating fragments are visible to the photodiode array. The signal in the 513 nm channel peaks and decays more quickly, which is consistent with a signal dominated by AlO molecular emission. The reduced extension in peak intensity for the second component indicates that AlO emission does not significantly increase as the ejecta cloud expands, which is consistent with the short lifetime of optical molecular emission and projectile-containing species primarily forming and emitting during the initial jetting phase.

At higher velocities relatively more radiating material is excavated from the target, meaning a lower proportion of emitting ejecta will correspond to the atomic/molecular emission from projectile-containing species. This implies that at a sufficiently high velocity the AlO molecular emission would no longer dominate the second component of the 513 nm channel and would appear more similar to decay profiles at other wavelengths. Additionally, this suggests that band-pass filters must be sufficiently narrow and centred at a wavelength corresponding to a peak in atomic/molecular emission in order to detect similar behaviour. It

is also worth noting that the impact flash is also highly dependent upon the angle of impact (Schultz 1996; Schultz *et al.*, 1996; Sugita & Schultz, 1999; Yafei *et al.*, 2019), and will likely alter the decay profile for impacts into frozen targets.

Conclusions

This study illustrates the considerable benefits of spectroscopically examining impact ejecta, which show a strong and varied wavelength dependence upon several impact parameters, with atomic/molecular emission influencing the temporal evolution of the ejecta flash. Future investigation of this wavelength dependence utilising a fully calibrated photodiode array may yield more reliable absolute detector intensities, which could be used to determine the temporal evolution of the ejecta temperature. Emission spectra from Al impacts into CO_2 ice and simulant-based targets show consistent contributions from AlO originating from the projectile. There appears to be very little or no emission that originates solely from the target material (e.g. CO emission), perhaps due to insufficient energy from the relatively small-scale impact. Despite this, these observations may provide a useful comparison for future observations of impact flashes on the moon, Mars and other frozen planetary bodies with a high surface composition of water or CO_2 ice.

The occurrence of multiple peaks within the impact flash decay profiles and differences in the segmented emission spectra indicate an inhomogeneous ejecta composition, as previously identified by Schultz and Eberhardy (2015) for impacts into powdered dolomite targets. A future comparison of flash decay profiles and emission spectra at different ejecta trajectories may therefore provide additional information regarding potential compositional changes at different locations around a crater site and determine a broader range of emitting atomic/molecular species present within the ejecta plume. The apparent strong correlation between target density and the rate-of-decay of the impact flash (in spectral regions without significant atomic/molecular emission) warrants further investigation using varied projectile and target materials. Such studies may assist in the determination of an underlying cause and potentially allow subsequent analyses to determine approximate densities of an unknown target material.

Changes in the initial flash intensity due to an increase in impact speed were shown to be wavelength independent. A strong, linear correlation is also shown between impact speed and decay exponent for CO_2 ice targets. Additionally, an increase in impact speed appears to maintain the duration of the flash's initial, short-lived peak, but alters the temporal behaviour of the secondary rise in emission intensity and its subsequent decay. These features also show a wavelength dependence, indicating further influence from strong atomic/molecular emission. These observations highlight the importance of using a wide range of impact parameters in both laboratory experiments and modelling when investigating complex ejecta phenomena.

Acknowledgements

The authors thank Prof. Peter Schultz and an anonymous reviewer for their helpful comments. We thank Dr Phillipa Timmins and Princeton Instruments for the loan of the high-speed spectrometer system. MCP, MJC and JT thank the STFC for help in funding this work.

JT thanks Wiktoria Fiolek and Yasin Malik for their assistance with the density measurements of the frozen targets. LA acknowledges receipt of a University of Kent GTA Scholarship. CA thanks ESA Science Faculty grant for building the detection instrument. The work of CA was supported by the French National Research Agency under the project “Investissements d’Avenir” UCA^{JEDI} with the reference number ANR-15-IDEX-01. The program “Flash!” of CA was supported by the Programme National de Planetologie (PNP) of CNRS/INSU, co-funded by CNES, and by the Crédits Scientifiques Incitatifs (CSI) of the Université Nice Sophia Antipolis.

References

Allen C.C., Jager K.M., Morris R.V., Lindstrom D.J., Lindstrom M.M., Lockwood J.P. 1998. Martian soil simulant available for scientific, educational study. *Earth and Space Science News* 79:405-409.

Ang J.A. 1990. Impact flash jet initiation phenomenology. *Int. J. Impact Eng.* 10:23-33.

Avdellidou C., Price M.C., Delbo M., Cole M.J. 2017, Survival of the impactor during hypervelocity collisions – II. An analogue for high-porosity targets. *MNRAS*, 464(1):734-738.

Avdellidou C., Vaubaillon J. 2019. Temperatures of lunar impact flashes: mass and size distribution of small impactors hitting the Moon, *MNRAS,* 484(4):5212-5222.

Bergeron N.P., Hollerman W.A., Goedeke S.M., Hovater M., Hubbs W., Finchum A., Moore R.J., Allison S.W., Edwards D.L. 2006. Experimental evidence of triboluminescence induced by hypervelocity impact. *Int. J. Impact. Eng.* 33:91-99.

Bruck Syal M., Schultz P.H., Crawford D.A. 2012. Impacts into porous and nonporous ice targets. *Geol. Soc. Amer.* (Charleston, N.C), Abstract 202-11.

Burchell M.J., Cole M.J., Ratcliff P.R. 1996. Light Flash and Ionization from Hypervelocity Impacts on Ice. *Icarus* 122:359-365.

Burchell M.J., Cole M.J., McDonnell J.A.M., Zarnecki J.C. 1999. Hypervelocity impact studies using the 2 MV Van de Graaff dust accelerator and two stage light gas gun of the University of Kent at Canterbury. *Measurement Science & Technology* 10:41-50.

Cudnik B.M., Dunham D.W., Palmer D.M., Cook A., Venable R., Gural P.S. 2003. Ground-based observations of lunar meteoritic phenomena. *Earth, Moon and Planets* 93:145-161.

Dunham D.W., Cudnik B., Palmer D.M., Sada P.V., Melosh J., Frankenberger M., Beech R., Pellerin L., Venable R., Asher D., Sterner R., Gotwols B., Wun B., Stockbauer D. 2000. The first confirmed video recordings of lunar meteor impacts. *Lunar Planet. Sci. XXXI*. Abstract 1547.

Eichhorn G. 1975. Measurements of the light flash produced by high velocity particle impact. *Planet. Space Sci.* 23:1519-1525.

Eichhorn G. 1976. Analysis of the hypervelocity impact process from impact flash measurements. *Planet. Space Sci.* 24:771-781.

Ernst C.M., Schultz P.H. 2003. Effect of initial conditions on impact flash decay. *Lunar Planet. Sci. XXXIV*. Abstract 2020.

Ernst C.M., Schultz, P.H., 2004. Early-time temperature of the impact flash and beyond. 2004. *Lunar Planet. Sci. XXXV*. Abstract 1721.

Ernst C.M., Schultz P.H. 2007. Evolution of the Deep Impact flash: Implications for the nucleus surface based on laboratory experiments. *Icarus* 190:334-344.

Ernst C.M., Barnouin O.S., Schultz P.H. 2011. Comparing experimental and numerical studies of the impact flash: Implications for impact melt generation. *EPSC Abstracts*, EPSC-DPS Joint Meeting 2011, 6:1484.

Gehring, J.W., Warnica R.L. 1963. An investigation of the phenomena of impact flash and its potential use as a hit detection and target discrimination technique. *Proc. 6th Hypervelocity Impact Symp.* 2:627-682.

Goel A., Lee N., Close S. 2015. Estimation of hypervelocity impact parameters from measurements of optical flash. *Int. J. Impact. Eng.* 84:54-63.

Häring H.-W., Ahner C., Belloni A. 2007. *Industrial Gases Processing*, Weinheim, Wiley-VCH.

Heunoske D., Schimmerohn M., Osterholz J., Schafer F. 2013. Time-resolved emission spectroscopy of impact plasma. *Procedia Engineering* 58:624-633.

Jean, B., Rollins T. L. 1970. Radiation from hypervelocity impact generated plasma, *AIAA J.* 8:1742-1748.

Kadono T., Fujiwara A. 1996. Observation of expanding vapor cloud generated by hypervelocity impact. *J. Geophys. Res.* 101:26097-26109.

Kondo K., Ahrens T.J. 1983. Heterogeneous shock-induced thermal radiation in minerals, *Phys. Chem. Miner.*, 9:173-181.

Kramida A., Ralchenko Y., Reader J., NIST ASD Team. 2019. *NIST Atomic Spectra Database* (ver. 5.7.1), Available: https://physics.nist.gov/asd [May 2020]. National Institute of Standards and Technology, Gaithersburg, MD. DOI: https://doi.org/10.18434/T4W30F.

Lawrence R.J., Reinhart W.D., Chhabildas L.C., Thornhill T.F. 2006. Spectral measurements of hypervelocity impact flash. *Int. J. Impact. Eng.* 33:353-363.

Martins Z, Price M.C, Goldman N., Sephton M.A., Burchell M.J. 2013. Shock synthesis of amino acids from impacting cometary and icy planet surface analogues. *Nature Geoscience,* 6:1045-1049.

McKay D.S., Carter J.L., Boles W.W., Allen C.C., Allton J.H. 1994. JSC-1: A new lunar soil simulant. *Proceedings from International Symposium on Engineering, Construction and Operations in Space IV*, ASCE, Reston, VA, 857-866.

Mihaly J.M., Tandy J.D., Adams M.A., Rosakis A.J. 2013. In situ diagnostics for a small-bore hypervelocity impact facility. *Int. J. Impact Eng.* 62:13-26.

Mihaly J.M., Tandy J.D., Rosakis, A.J., Adams M.A., Pullin D. 2015. Pressure-dependent, infrared-emitting phenomenon in hypervelocity impact. *J. Appl. Mech.* 82:011004.

Pearse R.W.B., Gaydon A.G. 1976. *The identification of molecular spectra*. 4th ed. Chapman and Hall, New York.

Pospieszalska M.K., Johnson R.E. 1991. Micrometeorite erosion of the main rings as a source of plasma in the inner saturnian plasma torus. *Icarus* 93:45-52.

Rager A.H., Smith E., Scheu B., Dingwell D.B. 2014. The effects of water vaporization on rock fragmentation during rapid decompression: Implications for the formation of fluidized ejecta on Mars. *EPSL* 385:68-78.

Schultz P.H. 1996. Effect of impact angle on vaporization. *J. Geophys. Res*. 101:21117-21136.

Schultz P.H., Adams M. A., Perry J. W., Goguen J. D., Sugita S., 1996. Impact flash spectroscopy. *Lunar Planet. Sci. XXVII*. 1149-1150.

Schultz P.H., Eberhardy C.A., Ernst C.M., A'Hearn M.F., Sunshine J.M., Lisse C.M. 2007. The Deep Impact oblique impact cratering experiment. *Icarus* 191:84-122.

Schultz P.H., Eberhardy C.A. 2015. Spectral probing of impact-generated vapor in laboratory experiments. *Icarus* 248:448-462.

Schultz P.H., Ernst C.M., Anderson J.L.B. 2005. Expectations for crater size and photometric evolution from the deep impact collision. Space Sci. Rev. 117:207-239.

Schultz P.H., Mustard J.F. 2004. Impact melts and glasses on Mars. *J. Geophys. Res.* 109: E01001.

Schultz P.H., Sugita S., Eberhardy C.A., Ernst C.M. 2006. The role of ricochet on impact vaporization. *Int. J. Impact Eng.* 33:771-780.

Suggs R.M., Moser D.E., Cooke W.J., Suggs R.J. 2014. The flux of kilogram-sized meteoroids from lunar impact monitoring. *Icarus*. 238:23-36.

Sugita S., Schultz P.H., Adams M. A. 1998. Spectroscopic measurement of vapor clouds due to oblique impacts. *J. Geophys. Res.* 103:19427-19441.

Sugita S., Schultz P.H. 1999. Spectroscopic characterization of hypervelocity jetting: Comparison with a standard theory. *J. Geophys. Res.* 104(E12):30825-30845.

Sugita S., Schultz P.H. 2003a. Interactions between impact-induced vapor clouds and the ambient atmosphere: 1. Spectroscopic observations using diatomic molecular emission. *J. Geophys. Res.* 108(E6):5051.

Sugita S., Schultz P.H. 2003b. Interactions between impact-induced vapor clouds and the ambient atmosphere: 2. Theoretical modelling. *J. Geophys. Res.* 108(E6):5052.

Sugita S., Schultz P.H., Hasegawa, S. 2003. Intensities of atomic and molecular bands observed in impact-induced luminescence. *J. Geophys. Res.* 108(E12):5140.

Sugita S., Schultz P.H., Hasegawa, S. 2004. What controls the intensity of impact-induced luminescence? *Lunar Planet. Sci. XXXV*. 1048.

Tandy J.D., Mihaly J.M., Adams M.A., Rosakis A.J. 2014. Examining the temporal evolution of hypervelocity impact phenomena via high-speed imaging and ultraviolet-visible emission spectroscopy. *J. Appl. Phys.* 116:034901.

Timmermann R., Grün E. 1991. Plasma emission from high velocity impacts of microparticles onto water ice. In *Origin and Evolution of Interplanetary Dust* (Levasseur-Regourd A.C. &

Hasegawa H., Eds.) *Proceedings, 126th Colloquium of the International Astronomical Union*. 173:375-378.

Tsembelis K., Burchell M.J., Cole M.J., Margaritis N. 2008. Residual temperature measurements of light flash under hypervelocity impact. *Int. J. Impact Eng.* 35:1368-1373.

Verreault J., Day J.P.R., Halswijk W.H.C., Loiseau J. Huneault J., Higgins A.J., Devir A.D. 2015. Emission spectroscopy of hypervelocity impacts on aluminum, organic and high-explosive targets. *Procedia Engineering* 103:618-627.

Vickery A.M. 1993. The theory of jetting: Application to the origin of tektites. *Icarus* 105:441-453.

Yafei H., Enling T., Liping H., Meng W., Kai G., Jin X., Jianjun M., Shuhua L., Ruizhi W., Zhenbo L. 2019. Evolutionary characteristics of thermal radiation induced by 2A12 aluminum plate under hypervelocity impact loading. *Int. J. Impact. Eng.* 125:173-179.

Yang W., Ahrens T.J., Miller G.H., Petach M. B. 1992. Jet ejecta mass upon oblique impact, in *Shock Compression of Condensed Matter*, edited by Schmidt S.C. *et al.*, North Holland, New York, 1011-1014.

Appendices

COMPONENT	JSC-1A LUNAR SIMULANT % WEIGHT	JSC-1 MARTIAN SIMULANT % WEIGHT
SiO_2	47.7	43.5
Al_2O_3	15.0	23.3
TiO_2	1.6	3.8
Fe_2O_3	3.4	15.6
MnO	-	0.3
CaO	10.4	6.2
K_2O	-	0.6
Na_2O	2.7	2.4
P_2O_5	-	0.9

Appendix A – Chemical composition of JSC-1A lunar (McKay *et al.*, 1994) and JSC-1 Martian (Allen *et al.*, 1998) regolith simulants.

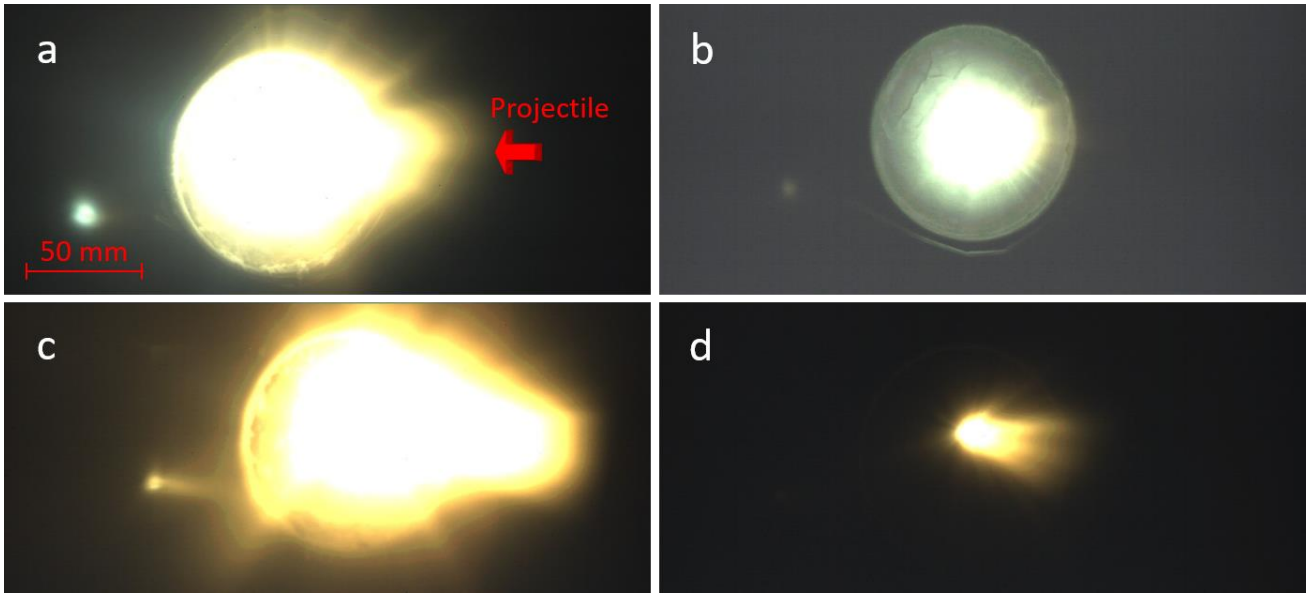

Appendix B – Impact flash photographs recorded from a 3 mm diameter Al projectile impacting solid targets of a) CO_2 ice, b) water ice, c) 50% CO_2 ice / 50% JSC-1A lunar regolith simulant, and d) 50% water ice / 50% JSC-1A lunar regolith simulant, corresponding to shots S1, S2, S5 and S6 respectively. The frame with greatest emission intensity for each target material was selected for comparison. Each photograph has an exposure time of approximately 0.35 ms, although exact timings of each frame relative to the impact time could not be determined. The bright area on the left side of images a), b) and c) are due to specular reflection from the steel can containing the frozen target. The edge of the steel can is also observed as the circular feature in these images.